PCCP

PAPER

Cite this: *Phys. Chem. Chem. Phys.*, 2017, **19**, 30883

Formation of C_2 oxygenates and ethanol from syngas on an Fe-decorated Cu-based catalyst: insight into the role of Fe as a promoter†

Lixia Ling,[ab] Qiang Wang,[a] Riguang Zhang,[c] Debao Li*[a] and Baojun Wang*[c]

Received 9th August 2017,
Accepted 1st November 2017

DOI: 10.1039/c7cp05411d

rsc.li/pccp

In this study, the formation mechanism of C_2 oxygenates and ethanol from syngas on Fe-decorated Cu bimetallic catalyst was investigated using density functional theory (DFT) calculations together with microkinetic modeling. The results showed that CH_2 was the most favored monomer among all the CH_x (x = 1–3) species over the FeCu bimetallic catalyst, which was more favorable than CH_3OH formation. Namely, the FeCu catalyst exhibited a good selectivity toward CH_2 formation instead of CH_3OH formation in syngas conversion. Starting from the CH_2 monomer, CH_2CO and CH_3CO *via* CO insertion into CH_2 and CH_2CO hydrogenation were the major products instead of C_2 hydrocarbons or methane, CH_3CO was successively hydrogenated to ethanol *via* CH_3CHO and CH_3CH_2O intermediates. Moreover, the microkinetic modeling showed that the FeCu bimetallic catalyst had a high selectivity toward ethanol rather than methanol and methane. Further, the addition of Fe into the Cu catalyst promoted CH_x formation by accelerating C–O bond cleavage, suppressed methanol formation, and facilitated C_2 oxygenate formation rather than methane formation, suggesting that the synergetic effect between Fe and Cu played an important role in the formation of C_2 oxygenates and ethanol. In addition, it is believed that the insights derived from this study can provide clues for the catalyst design of oxygenate synthesis and other bimetallic catalytic systems.

1 Introduction

Ethanol synthesis from syngas (CO and H_2) has attracted widespread interest,[1–4] as it can be used as an alternative transportation fuel or fuel additive for octane enhancement and as feedstock for value-added fine chemicals.[5–7] The catalysts reported for ethanol synthesis from syngas mainly include Rh-based catalysts,[8–10] Mo-based catalysts,[11,12] Cu-based catalysts,[13–19] and modified Fischer–Tropsch (F–T) synthesis catalysts.[20–23] Rh-based catalysts have shown good activity and selectivity toward ethanol formation, but the low CO conversion and very high price restrict their commercial utilization. Mo-based catalysts have been utilized at high pressures and temperatures although they have high selectivity toward ethanol formation. Also, a high productivity and selectivity toward ethanol formation at about 600 K and 13 MPa were found on the K_2CO_3/Co–MoS_2/clay catalyst.[24] Cu-based catalysts are less expensive than Rh-based and Mo-based catalysts; however, their low selectivity to ethanol is their major shortcoming. In our previous work,[13,19,25] we also demonstrated that the productivity and selectivity of ethanol was low on Cu(211), Cu(110), and Cu(100) surfaces, since methanol formation was more favorable than ethanol formation. Modified F–T synthesis catalysts are considered as promising candidates for ethanol synthesis from syngas, and in our previous work[10] we showed that introducing an Fe promoter into the Rh-based catalyst effectively increased ethanol productivity and selectivity. In addition, CuFe bimetallic catalysts are thought to be the most promising catalysts in syngas conversion to C_2 oxygenates due to their low cost, high activity, and selectivity.[21,26–28] As a result, CuFe bimetallic catalysts have been utilized to improve the total alcohol and C_{2+} alcohol selectivity in experimental and theoretical studies.[29–34]

CuFe bimetallic catalysts comprise two types: Cu-decorated Fe-based catalysts and Fe-decorated Cu-based catalysts. Nowadays, extensive studies are focused on Cu-decorated Fe-based catalysts. CO adsorption, dissociation as well as the C–C coupling on the

[a] *State Key Laboratory of Coal Conversion, Institute of Coal Chemistry, Chinese Academy of Science, Taiyuan 030001, Shanxi, P. R. China. E-mail: dbli@sxicc.ac.cn*

[b] *College of Chemistry and Chemical Engineering, Taiyuan University of Technology, Taiyuan 030024, Shanxi, People's Republic of China*

[c] *Key Laboratory of Coal Science and Technology of Ministry of Education and Shanxi Province, Taiyuan University of Technology, No. 79 West Yingze Street, Taiyuan 030024, Shanxi, P. R. China. E-mail: wangbaojun@tyut.edu.cn, wbj@tyut.edu.cn; Fax: +86 351 6041237; Tel: +86 351 6010898*

† Electronic supplementary information (ESI) available: The detailed descriptions about the adsorption of all the possible species involved in ethanol formation from syngas, the calculation methods about the activation barrier, reaction energy, the rate constant, and the microkinetic modeling over the FeCu(211) surface, as well as the differential charge density have been presented. See DOI: 10.1039/c7cp05411d

Cu-covered Fe(100) surface, show that the Cu monolayer-covered Fe(100) surface has a weaker CO adsorption and a much higher CO dissociation barrier, as well as easier C–C bond formation, compared to the clean Fe surface.[35,36] CO dissociation on the Cu-doped Fe(100) surfaces also suggested that Cu doping can reduce the activity of CO dissociation,[33] and act through a dual-site mechanism for higher alcohol synthesis on bimetallic catalysts.[37] The higher alcohol synthesis on the supported CuFe bimetallic catalysts was also investigated by Liu *et al.*,[32] who suggested that Cu-dispersed on an Fe catalyst with a high Fe/Cu molar ratio promoted the catalytic activity and facilitated the synthesis of higher alcohols.

For Fe-decorated Cu-based catalysts, a large number of experimental studies proved that a FeCu bimetallic catalyst with a Cu-rich composition could also show a high selectivity toward higher alcohols. The higher alcohols synthesis from syngas on Fe-modified $CuMnZrO_2$ catalysts was investigated by Xu *et al.*,[38] who suggested that enhancing the interaction between Cu and Fe can increase the catalytic activity in higher alcohol formation. The catalytic activity of CO hydrogenation and the selectivity toward higher alcohols presented an increasing trend with the gradual increase in the Fe concentration on an Fe-modified CuMnZnO catalyst, which may be attributed to the enhancement between the dispersed Cu and iron carbides.[39]

As mentioned above, extensive studies have reported that the CuFe bimetallic catalyst showed a good catalytic performance in higher alcohols synthesis. In the bimetallic catalytic, Cu was widely thought to facilitate the reduction of Fe^{3+} species to metallic Fe,[40] and Cu could also facilitate the conversion of magnetite to α-Fe under a H_2 atmosphere,[41,42] as well as Cu could significantly promote the reduction of Fe_2O_3 to metal Fe.[43] It was seen that the metallic Fe and Cu were the main species after the reduction by syngas.[44] The synergistic effect between Cu and Fe plays an important role in the high activity of mixed alcohol synthesis,[3,7,21,34,38] and CO adsorption and dissociation on CuFe alloy surfaces were faster than that on pure Cu.[45] To the best of our knowledge, the underlying formation mechanism of C_2 oxygenates from syngas and the role of Fe over FeCu bimetallic catalysts with a Cu-rich composition still remain unclear at a molecular level.

In this study, the underlying mechanism of the C_2 oxygenates and ethanol formation from syngas over FeCu bimetallic catalysts were examined using density functional theory (DFT) calculations together with microkinetic modeling, so that the role of Fe in the FeCu bimetallic catalyst in syngas conversion to C_2 oxygenates and ethanol can be clarified at a molecular level. Further, the results will not only help us better understand the underlying mechanism of C_2 oxygenates and ethanol formation from syngas over FeCu bimetallic catalysts, but can also give clues to aid the design and development of high-performance catalyst materials toward the desired products from syngas.

2 Computational details

2.1 Surface models

For FeCu bimetallic catalysts, there are two types of models: the adsorption model[34] and the substitution model.[33,36] Although the FeCu system has a rather large miscibility range,[46,47] there is no stable intermetallic Cu–Fe alloy phase in the phase diagram. Meanwhile, the adsorption models with Cu adsorbed on Fe surface have been widely investigated by previous studies,[34,48–51] suggesting that the FeCu bimetallic catalyst with an Fe-rich composition should follow the adsorption model instead of the substitution mode. As a result, for the FeCu bimetallic catalyst with a Cu-rich composition, the adsorption model was employed in this study.

Previous studies have proved that metal surfaces are full of surface defects under a realistic condition, which is significant to the properties of metals, especially, the surface reactivity.[52,53] In reality, the step site is the most common defect of metal catalysts, and it may play a key role in catalysis. Previous experiment studies[54] have investigated the higher alcohols synthesis from syngas, suggesting that higher alcohols can be produced with high selectivity over a CuFe binary catalyst. In this process, the atomic steps on the Cu surface induced by planar defects and lattice strain can serve as high-activity oxygenation sites. HRTEM observations have also provided further evidence that these types of planar defects are stacking faults and that twin boundaries consist of (100) and (111) surfaces.[54] Here, we try our best to present a representative model that includes the physical properties as mentioned above under realistic experimental conditions.

A stepped Cu(211) surface has the (111) terrace and (100)-type step, which shows a high activity in catalytic reactions.[55–57] The stepped surface shows a higher activity to CO[58] and O_2[59] dissociation than the flat surface. Additionally, C_2 oxygenates formation is also more favorable on the stepped Rh(211) surface than on the flat Rh(111) surface.[60] Besides, the stepped Cu(211) surface is more favorable for CO and CO_2 hydrogenation than that on the flat Cu(111) surface.[61] Therefore, the stepped Cu(211) surface was employed to model the Cu catalyst in this study.

Adsorptions of Fe atoms at different sites on the Cu(211) surface were examined, and it was found that the Fe atom preferred to be adsorbed at the hollow site with a high binding energy of 267.9 kJ mol^{-1}. Thus, an eight-layer $p(2 \times 3)$ slab model with Fe adsorbed at the hollow site on the Cu(211) surface was used to model the FeCu bimetallic catalyst (see Fig. 1). In order to ensure no significant interaction between slabs, a 15 Å vacuum spacing was set. The top five layers together with the adsorbed species were allowed to relax, while the bottom three layers were kept at their bulk position.

2.2 Computational methods

Periodic plane-wave spin-polarized density functional theory calculations were carried out by using the Vienna Ab-initio Software Package (VASP),[62,63] with the electron–ion interactions described by the projector-augmented wave (PAW) method.[64,65] In order to describe the exchange- correlation energies and potential, the generalized gradient approximation (GGA) proposed by Perdew and Wang (PW91)[66,67] was used in the calculations. Spin-polarized[68] calculations were performed for Fe systems, correctly accounting for the magnetic properties of Fe. The Brillouin zone was sampled by a $4 \times 4 \times 1$ *k*-points grid

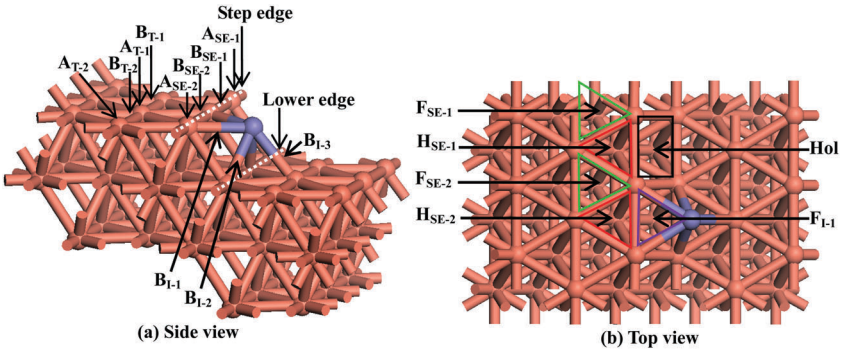

Fig. 1 Fe atom adsorbed on the Cu(211) surface; (a) side view, (b) top view. Orange and purple balls denote Cu and Fe atoms, respectively. A_{SE}, B_{SE}, F_{SE}, and H_{SE} refer to the atop, bridge, fcc, and hcp sites at the step edge (SE). A_T and B_T refer to the atop and bridge sites at the terrace, and Hol refers to the hollow site on the stepped surface. B_I and F_I refer to the bridge and fcc sites at the Fe–Cu interface.

generated *via* the Monkhorst–Pack procedure.[69,70] A plane-wave cutoff energy of 400 eV was adopted, which was widely used to investigate the adsorption and reaction on FeCu bimetallic catalysts.[33,36] In addition, a larger cutoff energy of 480 eV was also employed to calculate the adsorption and hydrogenation to CHO of CO on the FeCu(211) surface. The results indicated that the difference between the two adsorption energies with different cutoff energies was only 3.6 kJ mol^{-1}, and the energy barrier difference for forming CHO was 4.1 kJ mol^{-1}. Besides, the bonds lengths of Fe–C and C–O were 1.746 and 1.174 Å for CO adsorption with a cutoff energy of 480 eV, which were similar to the values of 1.747 and 1.176 Å with a cutoff energy of 400 eV. This implies that the parameters used in this work are feasible. The geometry optimization was allowed to converge when the energy difference between two consecutive steps was less than 5×10^{-6} eV, and the forces for ions were lower than 0.01 eV $Å^{-1}$.

Transition states were located by combining the Climbing-image Nudged Elastic Band method (CI-NEB)[71,72] and dimer method.[73,74] A linear interpolation between reactant and product states was used to find the saddle points between the known reactants and products for all the NEB calculations, and the initial guess for the transition state structure was optimized using the dimer method. In this study, the forces for all the atoms of the optimized transition state structure using the dimer method were less than 0.05 eV $Å^{-1}$. The transition states were further confirmed by a vibrational frequency calculation, in which only one imaginary frequency was obtained at the saddle point.

3 Results and discussion

3.1 Adsorption of all the possible species

The adsorption energy with the zero-point vibrational energy (ZPE) correction and the key geometrical parameters of the reaction intermediates involved in ethanol formation from syngas on the FeCu(211) surface are listed in Table 1. The corresponding most stable adsorption configurations are presented in Fig. 2. The detailed descriptions are shown in the ESI.†

The results show that all the intermediates species prefer to interact with Fe atoms or the sites consisting of Fe and Cu atoms. Meanwhile, Bader charge analysis shows that the average charge transfer between neighboring Fe and Cu atoms is 0.15 *e*, which enhanced the adsorption of all the intermediates species.

3.2 Mechanism of ethanol formation from syngas

In this section, all the possible elementary reactions involved in ethanol formation from syngas were examined, and the activation barrier with ZPE correction, the reaction energy with ZPE correction, and the rate constant (details are presented in the ESI†) were calculated to obtain the preference mechanisms of ethanol formation from syngas.

The FeCu bimetallic catalyst exhibited good catalytic activity in syngas conversion at the temperature range of 500–600 K;[20,75] thus, the rate constants of the elementary reactions involved in ethanol formation from syngas were calculated using the harmonic transition state theory[76] at 500, 525, 550, 575 and 600 K, respectively.

3.2.1 CO hydrogenation and dissociation. Previous studies found that the initial activation of CO was of major importance for understanding the formation of the CH_x intermediate.[77–79] Thus, the initial activation of CO was investigated and was found to involve CO dissociation and hydrogenation, specifically the direct dissociation of CO and CO hydrogenation to COH and CHO. Fig. 3 presents the potential energy diagram of the above reactions together with the initial states (ISs), transition states (TSs), and final states (FSs).

CO directly dissociates to form C and O atoms *via* TS1 in R1, in which the C atom adsorbs at the F_{I-1} site, and the O atom is connected with an Fe atom with the C–O distance of 2.076 Å. This reaction is endothermic by 111.8 kJ mol^{-1}, and the activation barrier is 252.6 kJ mol^{-1}, with a reaction rate constant of 8.22×10^{-14} s^{-1} at 500 K (here, we only present the rate constant at 500 K in Table 2, while those at the other temperatures are listed in Table S1, ESI†). CO can undergo H atom interactions with an O atom and C atom leading to COH and CHO in R2 and R3, respectively. Activation barriers of 172.2 and 102.1 kJ mol^{-1} are needed for these two hydrogenation processes *via* TS2 and TS3, which are lower than that of the direct dissociation process. This implies that the H-assisted reaction is easier than the

Table 1 Adsorption energy with the zero-point vibrational energy (ZPE) correction and key geometrical parameters (Å) of all the possible intermediates involved in ethanol formation from syngas on the FeCu(211) surface

Species	E_{ads} (kJ mol^{-1})	Configuration	Key parameters (Å)
C	694.6	F_{I-1}	Fe–C: 1.612; Cu–C: 1.938, 1.939
H	261.3	Atop-Fe	Fe–H: 1.630
O	627.7	F_{I-1}	Fe–O: 1.717; Cu–O: 1.978
OH	397.2	B_{I-1}	Fe–O: 1.831; Cu–O: 2.116
CO	234.7	Atop-Fe	Fe–C: 1.747; C–O: 1.176
CH	633.0	F_{I-1}	Fe–C: 1.720; Cu–C: 1.997, 1.999
CH_2	435.8	B_{I-1}	Fe–C: 1.793; Cu–C: 2.065
CH_3	245.1	Atop-Fe	Fe–C: 1.896
CHO	301.0	Atop-Fe *via* C and O	Fe–C: 1.799; Fe–O: 1.945
CH_2O	201.3	Atop-Fe *via* C and O	Fe–C: 2.073; Fe–O: 1.767
CH_3O	339.9	Atop-Fe *via* O	Fe–O: 1.717
COH	434.5	F_{I-1} *via* C	Fe–C: 1.711; Cu–C: 2.091, 2.092
CHOH	347.7	Atop-Fe *via* C	Fe–C: 1.791
CH_2OH	256.1	Atop-Fe *via* C and O	Fe–C: 1.939; Fe–O: 1.980
CH_3OH	100.9	Atop-Fe *via* O	Fe–O: 1.979
H_2O	63.7	Atop-Fe *via* O	Fe–O: 1.997
CH_4	32.0	Atop-Fe	Fe–C: 2.183
C_2H_4	165.2	Atop-Fe	Fe–C_1: 2.076; Fe–C_2: 1.990
C_2H_6	51.6	Atop-Fe	Fe–C_1: 2.136; Fe–C_2: 2.120
CH_2CO	197.6	B_{I-1} *via* C_1[a], C_2 and O	Fe–C_1: 1.842; Fe–C_2: 1.940; Cu–C_1: 2.059
CH_2COH	330.5	Atop-Fe *via* C_1 and C_2	Fe–C_1: 1.776; Fe–C_2: 2.005
CH_2CHO	308.2	B_{I-1} *via* C_1, C_2 and O	Fe–C_1: 1.999; Fe–C_2: 2.034; Fe–O: 1.941; Cu–O: 2.127
CH_3CO	302.1	B_{I-1} *via* C_1 and O	Fe–C_1: 1.811; Cu–O: 2.091
CH_3COH	326.2	Atop-Fe *via* C_1	Fe–C_1: 1.776
CH_3CHO	170.6	B_{I-1} *via* C_1 and O	Fe–C_1: 1.982; Fe–O: 1.876; Cu–O: 2.193
CH_3CHOH	242.2	Atop-Fe *via* C_1 and O	Fe–C_1: 1.925; Cu–O: 2.049
CH_3CH_2O	338.5	Atop-Fe *via* O	Fe–O: 1.712
C_2H_5OH	100.6	Atop-Fe *via* O	Fe–O: 1.967

[a] C_1 denotes the C atom linked with functional groups.

direct dissociation, in which CO hydrogenation to CHO is more favorable than the other pathway with an activation barrier of 102.1 kJ mol^{-1}, as shown in Fig. 3. CHO species, as the dominant product of the initial activation of CO, was also investigated on Cu(211),[13] Cu(110),[25] Cu(100),[19] and MnCu(211) surfaces.[80] In addition, the barrier of CO hydrogenation to CHO on the FeCu(211) surface is also lower than that on the Cu(211) surface (108.1 kJ mol^{-1}),[13] suggesting that the addition of Fe can enhance the catalytic activity toward CO activation. Additionally, Fe alone is known to be active in breaking the C–O bond,[34,37] which is the prerequisite for initiating CH_x formation.

On the other hand, previous studies about CO hydrogenation reactions have not considered the effect of the presence of H atoms on the reaction mechanism.[80–85] However, the calculated results can clarify the reaction mechanism. Moreover, although a lot of energetically more stable H species exist on the surface in the hydrogenation reaction, when the hydrogenation reaction occurs under a realistic condition, only one H adatom interacts with the corresponding adjacent adsorbed species. Thus, the effect of the presence of H atoms on the reaction mechanism can be negligible under a realistic condition. As a result, all the different hydrogenation steps involve the addition of atomic hydrogen on the surface, and only one H atom was present on the surface for each hydrogenation step in this study.

3.2.2 Correlated reactions of CHO. The above results show that CHO is the major product for the initial activation of CO on the FeCu(211) surface; thus, CH formation (R4–R6) is examined here on the basis of CHO species. CHO hydrogenation to CH_2O (R7) is also considered.

CHO directly dissociates to form CH and O *via* TS4 with an activation barrier of 85.2 kJ mol^{-1} in R4, and a reaction rate constant of 8.35×10^3 s^{-1}. CH is adsorbed at the F_{I-1} site, while an O atom is adsorbed at the atop-Fe site with a C–O distance of 1.932 Å in TS4. CH can also be formed by CHO hydrogenation *via* a CHOH intermediate. The formation of CHOH *via* TS5 has an activation barrier of 136.1 kJ mol^{-1} in R5. The following C–O bond scission of CHOH can form CH and OH *via* TS6 in R6. This elementary reaction is exothermic by 104.2 kJ mol^{-1}, with an activation barrier of 42.9 kJ mol^{-1} and a reaction rate constant of 6.05×10^7 s^{-1}. CHO hydrogenation may also occur leading to CH_2O, with a low activation barrier of 12.2 kJ mol^{-1} *via* TS7 (R7), in which CHO and a H atom are adsorbed at the atop-Fe site with a C–H distance of 1.452 Å. The reaction energy is −10.5 kJ mol^{-1} for the CHO hydrogenation.

As presented in Fig. 4, among two pathways of CH formation, CHO → CH + O is the most favorable pathway with an activation barrier of 85.2 kJ mol^{-1}, which is lower by 50.9 kJ mol^{-1} than the pathway of CHO + H → CHOH → CH + OH. However, CHO direct dissociation is still more unfavorable than CHO hydrogenation to CH_2O with a low activation barrier of 12.2 kJ mol^{-1}. Thus, the preferred product starting from CHO species should be CH_2O.

3.2.3 Correlated reactions of CH_2O. As mentioned above, CH_2O is the dominant species in CHO hydrogenation on the FeCu(211) surface; thus, CH_2 formation (R8–R10) based on

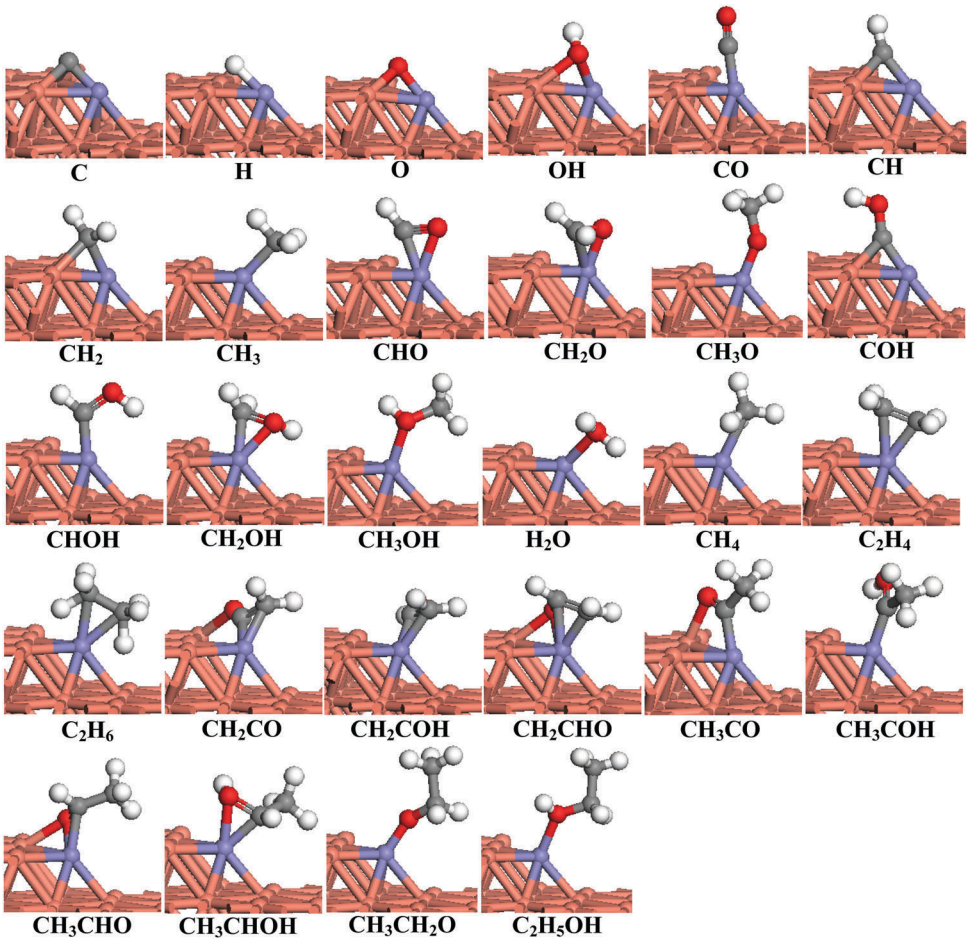

Fig. 2 The most stable adsorption configurations of the reactants and possible intermediates involved in ethanol formation from syngas on the FeCu(211) surface. C, O, H, Cu, and Fe atoms are shown by the gray, red, white, orange, and purple balls, respectively.

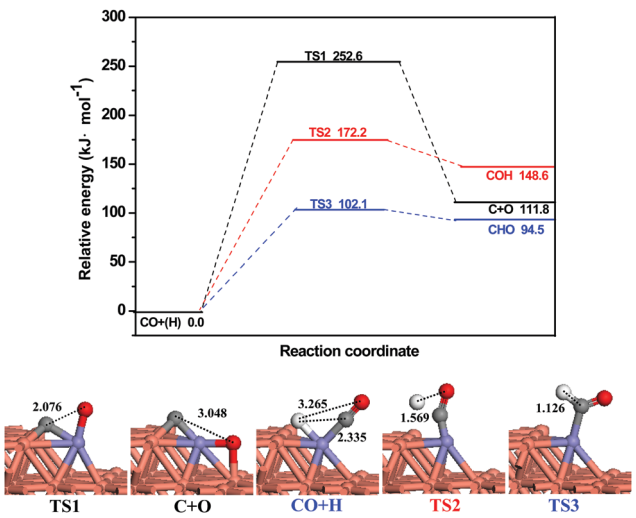

Fig. 3 Potential energy profile of CO dissociation and hydrogenation, together with the structures of ISs, TSs, and FSs on the FeCu(211) surface. Bond lengths are in Å.

CH_2O species is considered here. CH_2O hydrogenation to CH_3O (R11) is also examined.

CH_2O direct dissociation into CH_2 and O *via* TS8 needs to overcome an activation barrier of 77.5 kJ mol^{-1}, while the reaction rate constant is 2.25 × 10^5 s^{-1} in R8. CH_2 adsorbs at the Fe–Cu bridge site, and the O atom adsorbs at the atop-Fe atom with a C–O distance of 2.048 Å in TS8.

CH_2O hydrogenation can lead to the formation of CH_2 and OH *via* a CH_2OH intermediate, where activation barriers of 56.6 and 38.1 kJ mol^{-1} are needed to be overcome *via* TS9 and TS10, respectively. CH_2O hydrogenation may also form CH_3O *via* TS11 with an activation barrier of 59.5 kJ mol^{-1} and a reaction rate constant of 3.75 × 10^7 s^{-1}. CH_2O and H atom adsorb at the atop-Fe atom site with an O–H distance of 1.502 Å in TS11.

Starting from CHO + H species, the pathways of CH_2O → CH_2 + O (R8) and CH_2O + H → CH_2OH → CH_2 + OH (R9, R10) have the highest barriers of 67.0 and 67.4 kJ mol^{-1}, respectively. However, higher energy barriers of 157.4 and 158.3 kJ mol^{-1} need to be overcome on the Cu(211) surface for the same steps,[13] implying that FeCu(211) can enhance the catalytic activity toward CH_2 formation. Meanwhile, the rate-determining steps of these two pathways are CH_2O → CH_2 + O and CH_2O + H → CH_2OH with rate constants of 2.25 × 10^5 and 2.96 × 10^7 s^{-1}, respectively. As a result, the most favorable pathway for CH_2 formation is CH_2O + H → CH_2OH → CH_2 + OH. On the other hand, CH_2O

Table 2 Possible elementary reactions involved in ethanol formation from syngas, together with the activation energies (E_a), reaction energies (ΔE), and the rate constants at 500 K, as well as the imaginary frequency (cm^{-1}) corresponding to the transition state on the FeCu(211) surface

	Elementary reactions	Transition state	E_a (kJ mol^{-1})	ΔE (kJ mol^{-1})	k (s^{-1})
R1	$CO \rightarrow C + O$	TS1	252.6	111.8	8.22×10^{-14}
R2	$CO + H \rightarrow COH$	TS2	172.2	148.6	8.57×10^{-6}
R3	$CO + H \rightarrow CHO$	TS3	102.1	94.5	1.42×10^{4}
R4	$CHO \rightarrow CH + O$	TS4	85.2	−52.0	8.35×10^{3}
R5	$CHO + H \rightarrow CHOH$	TS5	136.1	76.1	1.20×10^{-1}
R6	$CHOH \rightarrow CH + OH$	TS6	42.9	−104.2	6.05×10^{7}
R7	$CHO + H \rightarrow CH_2O$	TS7	12.2	−10.5	2.14×10^{12}
R8	$CH_2O \rightarrow CH_2 + O$	TS8	77.5	−6.2	2.25×10^{5}
R9	$CH_2O + H \rightarrow CH_2OH$	TS9	56.6	39.8	2.96×10^{7}
R10	$CH_2OH \rightarrow CH_2 + OH$	TS10	38.1	−83.9	1.67×10^{9}
R11	$CH_2O + H \rightarrow CH_3O$	TS11	59.5	2.2	3.75×10^{7}
R12	$CH_3O \rightarrow CH_3 + O$	TS12	123.7	−24.0	8.05
R13	$CH_3O + H \rightarrow CH_3OH$	TS13	105.8	66.2	2.01×10^{3}
R14	$CH_2OH + H \rightarrow CH_3OH$	TS14	87.7	13.0	6.84×10^{3}
R15	$CH_2 \rightarrow CH + H$	TS15	73.5	38.0	1.00×10^{5}
R16	$CH_2 + H \rightarrow CH_3$	TS16	42.7	−22.9	8.1×10^{8}
R17	$CH_2 + CH_2 \rightarrow C_2H_4$	TS17	61.8	−58.7	1.91×10^{7}
R18	$CH_2 + CO \rightarrow CH_2CO$	TS18	40.2	−14.1	4.80×10^{8}
R19	$CH_2 + CHO \rightarrow CH_2CHO$	TS19	48.4	−66.7	1.40×10^{8}
R20	$CH_3 \rightarrow CH_2 + H$	TS20	65.5	22.9	8.92×10^{5}
R21	$CH_3 + H \rightarrow CH_4$	TS21	83.2	−16.9	1.73×10^{4}
R22	$CH_3 + CH_3 \rightarrow C_2H_6$	TS22	155.9	15.7	6.09×10^{-4}
R23	$CH_3 + CO \rightarrow CH_3CO$	TS23	75.4	37.5	3.36×10^{5}
R24	$CH_3 + CHO \rightarrow CH_3CHO$	TS24	75.5	−48.8	8.95×10^{5}
R25	$CH_2CO + H \rightarrow CH_3CO$	TS25	12.9	4.5	3.98×10^{12}
R26	$CH_2CO + H \rightarrow CH_2CHO$	TS26	84.5	6.1	1.24×10^{5}
R27	$CH_2CO + H \rightarrow CH_2COH$	TS27	77.3	35.3	3.64×10^{5}
R28	$CH_3CO + H \rightarrow CH_3CHO$	TS28	84.2	53.1	7.43×10^{5}
R29	$CH_3CO + H \rightarrow CH_3COH$	TS29	96.3	26.2	1.33×10^{4}
R30	$CH_3CHO + H \rightarrow CH_3CH_2O$	TS30	22.4	−5.8	1.20×10^{11}
R31	$CH_3CHO + H \rightarrow CH_3CHOH$	TS31	59.9	24.5	4.56×10^{6}
R32	$CH_3CH_2O + H \rightarrow C_2H_5OH$	TS32	114.1	73.6	2.40×10^{1}

hydrogenation to CH_3O has an activation barrier of 59.5 kJ mol^{-1} and a rate constant of 3.75×10^{7} s^{-1}, which is competitive to the formation of CH_2OH. As a result, both CH_2OH and CH_3O intermediates are more likely to be formed by CH_2O hydrogenation (Fig. 5).

3.2.4 CH_3 and CH_3OH formation. Both CH_2OH and CH_3O are the favorable species from CH_2O hydrogenation on the FeCu(211) surface according to the above analysis. Thus, CH_3O direct dissociation to form CH_3 (R12), as well as CH_3O and CH_2OH hydrogenation to CH_3OH (R13, R14) are examined here.

The direct C–O bond cleavage of CH_3O *via* TS12 leads to the formation of CH_3, where an activation barrier of 123.7 kJ mol^{-1} is needed to be overcome, and the reaction rate constant is 8.05 s^{-1}. CH_3 and O are adsorbed at the atop-Fe site with a C–O distance of 1.973 Å in TS12.

About the formation of CH_3OH, both CH_3O hydrogenation and CH_2OH hydrogenation are feasible. An activation barrier of 105.8 kJ mol^{-1} and a reaction rate constant of 2.01×10^{3} s^{-1} are involved in CH_3O hydrogenation, while an activation barrier of 87.7 kJ mol^{-1} and a reaction rate constant of 6.84×10^{3} s^{-1} are involved in CH_2OH hydrogenation.

As illustrated in Fig. 6, beginning with CHO + H species, the pathway for CH_3 formation has the highest barrier of 115.4 kJ mol^{-1}, which is higher than CH_3O hydrogenation to CH_3OH. In addition, the barrier for CH_3 formation on the FeCu(211) surface is also lower than that on the MnCu(211) surface (203.7 kJ mol^{-1}).[78]

3.2.5 The most favorable CH_x (x = 1–3), and CH_3OH formation. According to the above discussion about the formation of different species, the most favorable formation pathways for CH_x (x = 1–3) species and CH_3OH starting from CHO + H species are shown in Fig. 7.

For CH formation, $CHO \rightarrow CH + O$ is the most feasible pathway with the highest barrier of 85.2 kJ mol^{-1} and a rate constant of 8.35×10^{3} s^{-1}. The most favorable pathway is $CHO + H \rightarrow CH_2O + H \rightarrow CH_2OH \rightarrow CH_2 + OH$ for CH_2 formation, in which $CH_2O + H \rightarrow CH_2OH$ is the rate-determining step, with a rate constant of 2.96×10^{7} s^{-1}. For CH_3 formation, the pathway of $CHO + H \rightarrow CH_2O + H \rightarrow CH_3O \rightarrow CH_3 + O$ has the highest barrier of 115.4 kJ mol^{-1}, and $CH_3O \rightarrow CH_3 + O$ is the rate-determining step, with a rate constant of 8.05 s^{-1}. $CHO + H \rightarrow CH_2O + H \rightarrow CH_3O + H \rightarrow CH_3OH$ is favorable for CH_3OH formation, in which $CH_3O + H \rightarrow CH_3OH$ is the rate-determining step, with a rate constant of 2.01×10^{3} s^{-1}, which is more than 200 times that of CH_3O dissociation.

Therefore, among all the CH_x (x = 1–3) species, CH_2 is the most favored monomer, and is also more favorable than CH_3OH formation, both thermodynamically and kinetically. Namely, the FeCu(211) surface exhibits a good selectivity toward CH_2 formation instead of CH_3OH formation in syngas conversion. However, previous studies have proved that CH_3 species are the most favored monomer on the Cu(211) surface,[13] indicating that the Cu(211) surface provides few CH_x monomers to participate

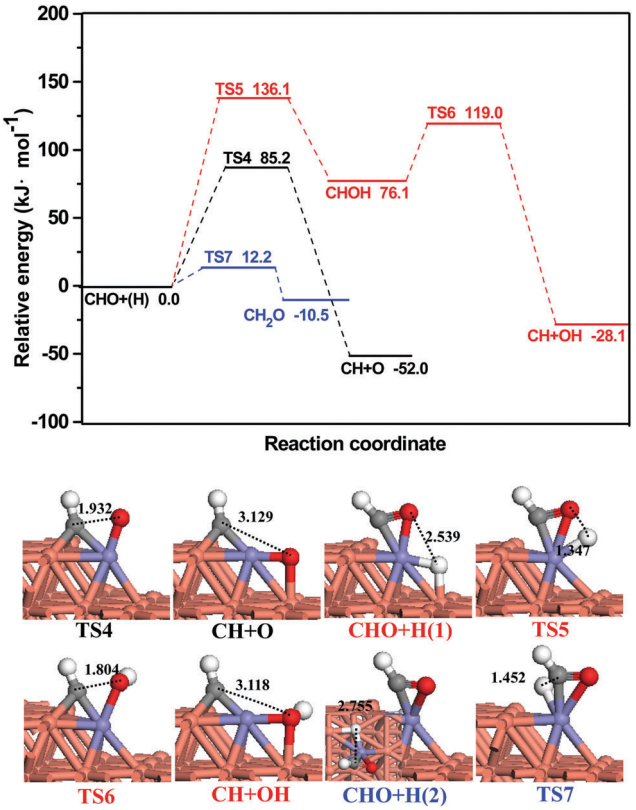

Fig. 4 Potential energy profile of CHO dissociation and hydrogenation, together with the structures of ISs, TSs, and FSs on the FeCu(211) surface. Bond lengths are in Å.

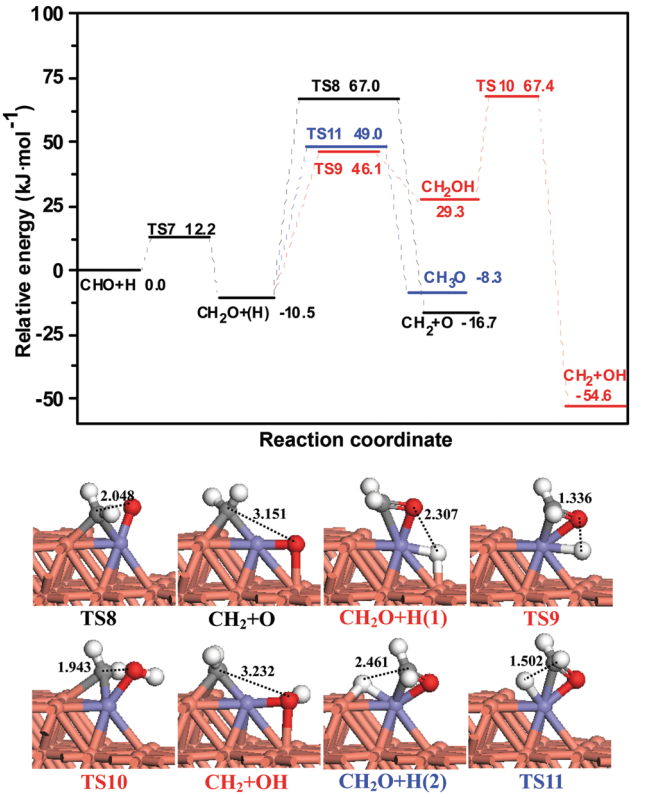

Fig. 5 Potential energy profile of CH_2O dissociation and hydrogenation, together with the structures of ISs, TSs, and FSs on the FeCu(211) surface. Bond lengths are in Å.

in C–C chain formation; namely, the Cu catalyst exhibits a good selectivity toward CH_3OH formation rather than ethanol. As a result, compared to the Cu catalyst, the addition of Fe as a promoter into the Cu catalyst clearly improves the selectivity toward CH_2 formation instead of CH_3OH formation, which is consistent with the previous experimental studies.[39]

3.3 C_2 Oxygenates and ethanol formation

From the above discussion, we can see that the CH_2 monomer is the dominant form of CH_x (x = 1–3) species from syngas on the FeCu(211) surface; hence, C_2 oxygenate formation *via* CO and CHO insertion are considered here. Meanwhile, CH_2 hydrogenation, dissociation, and coupling are also examined. The potential energy profile of the reactions related to CH_2 species together with the corresponding structures are presented in Fig. 8.

CH_2 dissociation into CH and H *via* TS15 has an activation barrier and reaction energy of 73.5 and 38.0 kJ mol^{-1} in R15, and a reaction rate constant of 1.00×10^5 s^{-1}. CH_2 hydrogenation to CH_3 *via* TS16 needs to overcome an activation barrier of 42.7 kJ mol^{-1} with a reaction rate constant of 8.1×10^8 s^{-1} for R16. CH_2 is adsorbed at the $B_{I\text{-}1}$ site, An H atom is adsorbed at the atop-Fe site, with the distance between the C and H atoms being 1.705 Å in TS16. In addition, CH_2 self-coupling to C_2H_4 was also investigated, and an activation barrier of 61.8 kJ mol^{-1} was needed to be overcome. Certainly, CO can insert into CH_2, leading to CH_2CO *via* TS18, where this elementary reaction is slightly exothermic by 14.1 kJ mol^{-1} with an activation barrier of 40.2 kJ mol^{-1} for R18, and a reaction rate constant of 4.80×10^8 s^{-1}. In TS18, CH_2 and CO species are adsorbed at the $A_{SE\text{-}2}$ Cu site and $B_{I\text{-}1}$ Fe–Cu site with a C–C distance of 2.910 Å. When CHO inserts into CH_2, CH_2CHO is formed *via* TS19. The activation barrier is 48.4 kJ mol^{-1} with a reaction rate constant of 1.40×10^8 s^{-1}.

Among all the reactions related to CH_2 species shown in Fig. 8, CO insertion into CH_2 to CH_2CO (R18) with an activation barrier of 40.2 kJ mol^{-1} is the most favorable in terms of kinetics. Meanwhile, CH_2 hydrogenation to CH_3 (R16) has an activation barrier of 42.7 kJ mol^{-1}, which is competitive with CH_2CO formation. As a result, CH_3 and CH_2CO are the major products among the reactions related to CH_2 species. In the following paragraphs, the correlated reactions of CH_3 and CH_2CO are studied.

Reactions related to CH_3 species are shown in Fig. 9, where it can be seen that CH_3 dissociation (R20) has the smallest activation barrier of 65.6 kJ mol^{-1}, which is the reverse reaction of R16, and TS20 is the same as TS16. CO inserts into CH_3, leading to the formation of CH_3CO (R23), with an activation barrier of 75.4 kJ mol^{-1} needed to be overcome, which is lower than that on the Cu(211) surface, with an energy barrier of 141.0 kJ mol^{-1}.[13] CH_3 hydrogenation to CH_4 (R21) has an activation barrier of 83.2 kJ mol^{-1}. CH_3 self-coupling (R22) and CHO insertion

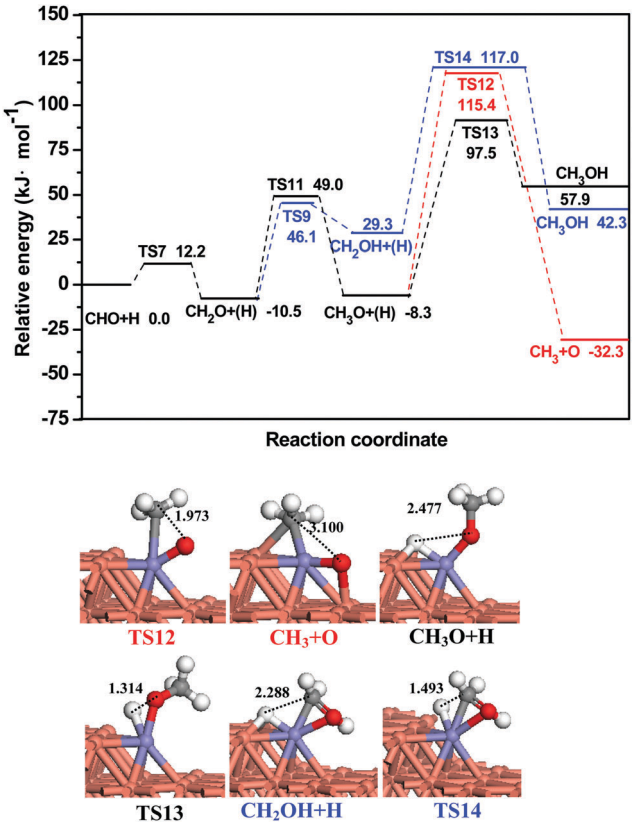

Fig. 6 Potential energy profile of CH_3 and CH_3OH formation on the FeCu(211) surface, together with the structures of the partial initial states, transition states, and final states. Bond lengths are in Å.

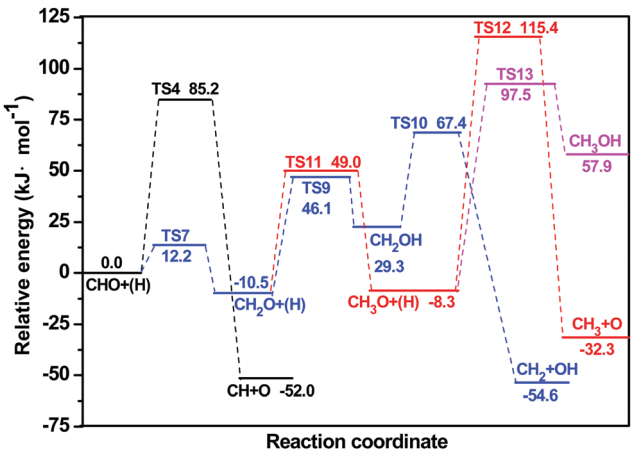

Fig. 7 Potential energy diagram of the most favorable formation pathways for CH_x (x = 1–3) and CH_3OH beginning with the initial state CHO + H on the FeCu(211) surface.

into CH_3 to CH_3CHO (R24) are difficult to proceed due to the high activation barriers of 155.9 and 75.5 kJ mol^{-1}, respectively. They are also hard to proceed on the Cu(211) surface with activation barriers of 238.2 and 87.9 kJ mol^{-1}, respectively.[13] It can be seen that CH_3 prefers to be dissociated into CH_2, and meanwhile, a small quantity of CH_3CO and CH_4 can be formed, and CH_3CO can be successively hydrogenated to ethanol.

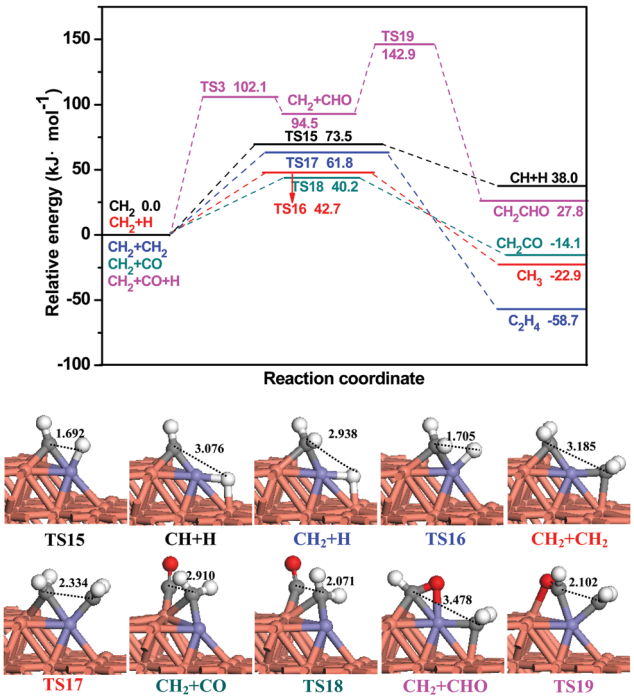

Fig. 8 Potential energy profile of CH_2 hydrogenation, dissociation, and coupling and CO/CHO insertion, together with the structures of ISs, TSs, and FSs on the FeCu(211) surface. Bond lengths are in Å.

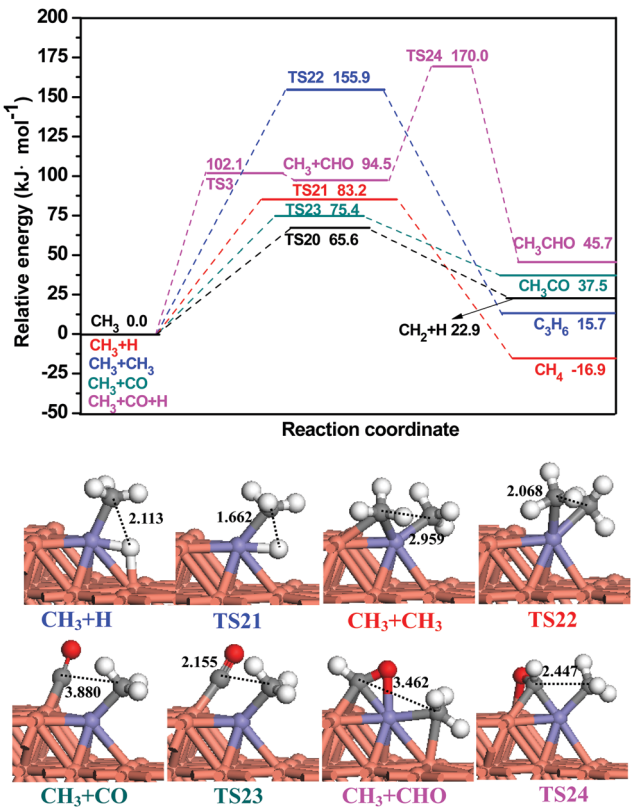

Fig. 9 Potential energy profile of CH_3 hydrogenation, dissociation, and coupling and CO/CHO insertion, together with the structures of ISs, TSs, and FSs on the FeCu(211) surface. Bond lengths are in Å.

As mentioned above, CH_2 and CH_3 species can transform each other, and are also the main CH_x species on the FeCu(211) surface, which is similar to the case on the CoCu(211) surface.[18] The dominant C_2 oxygenates are CH_2CO and CH_3CO, and CH_4 is formed as the byproduct. However, CH_3CHO is the major C_2 oxygenate on the MnCu(211) surface by CHO insertion into CH_3.[78] Then, both CH_2CO and CH_3CO can be successively hydrogenated to C_2H_5OH. The potential energy profile of ethanol formation, together with the structures of ISs and TSs, is shown in Fig. 10.

Staring from CH_2CO, three hydrogenation species can be obtained. First, CH_2CO hydrogenation to CH_3CO (R25) *via* TS25 has an activation barrier of 12.9 kJ mol^{-1} with a reaction energy of 4.5 kJ mol^{-1} and a rate constant of 3.98×10^{12} s^{-1}. CH_2CO and H are adsorbed at the Fe–Cu bridge and the atop-Fe site in TS25, respectively. The distance between C_α and H atom is decreased to 1.695 Å from 2.345 Å in the initial state, CH_2CO + H(1). Second, CH_2CO can also be hydrogenated, leading to CH_2CHO (R26) *via* TS26, where an activation barrier of 84.5 kJ mol^{-1} is needed to be overcome with a reaction energy of 6.1 kJ mol^{-1} and a rate constant of 1.24×10^5 s^{-1}. Third, CH_2CO hydrogenation to CH_2COH (R27) *via* TS27 has an activation barrier of 77.3 kJ mol^{-1} with a reaction energy of 35.3 kJ mol^{-1} and a rate constant of 3.64×10^5 s^{-1}. We can see that that CH_2CO prefers to be hydrogenated to CH_3CO.

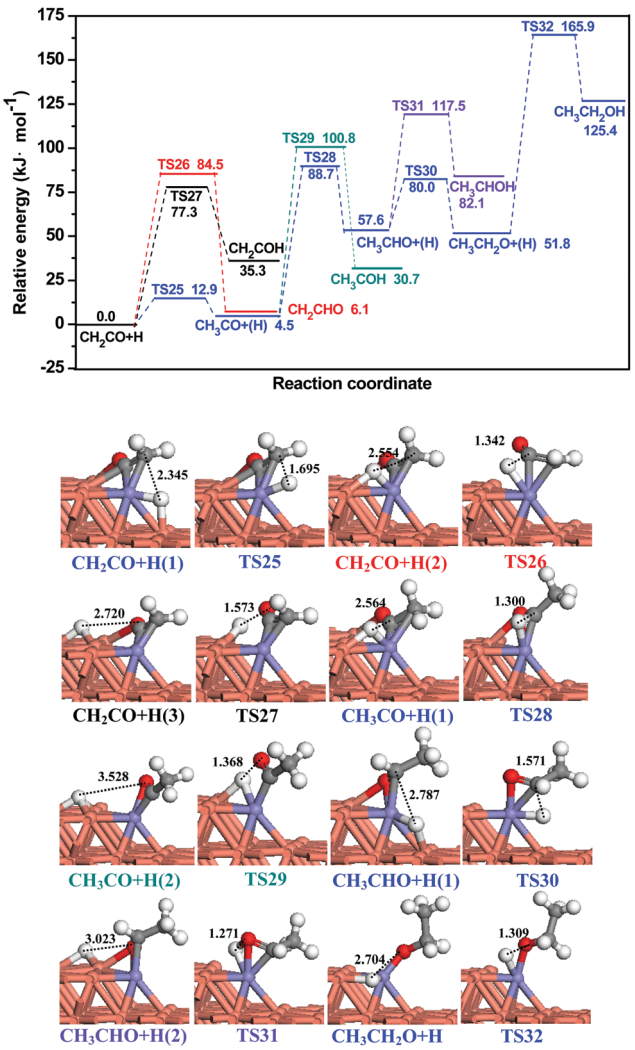

Fig. 10 Potential energy profile of the hydrogenation of C_2 oxygenates to ethanol, together with the structures of ISs, TSs, and FSs on the FeCu(211) surface. Bond lengths are in Å.

CH$_3$CO hydrogenates to form CH_3CHO (R28) *via* TS28, where this elementary reaction has an activation barrier of 84.2 kJ mol^{-1}, which is lower than that on the Cu(211) surface with a value of 171.9 kJ mol^{-1}.[13] In TS28, CH_3CO is adsorbed at the Fe–Cu bridge site, and H is adsorbed at the atop-Fe site. The distance between the C_α and H atom is decreased to 1.300 Å from 2.564 Å in the initial state, CH_3CO + H(1). CH_3CO may hydrogenate to form CH_3COH (R29) *via* TS29, and has an activation barrier of 96.3 kJ mol^{-1} with a rate constant of 1.33×10^4 s^{-1}. CH_3CO is adsorbed at the atop-Fe site, and H is adsorbed at the Fe–Cu bridge site in TS29. Thus, CH_3CO prefers to be hydrogenated to CH_3CHO.

Starting from CH_3CHO, CH_3CHO hydrogenation to CH_3CH_2O (R30) has an activation barrier of 22.4 kJ mol^{-1} with a rate constant of 1.20×10^{11} s^{-1}. CH_3CHO can also hydrogenate to CH_3CHOH (R31) with an activation barrier of 59.9 kJ mol^{-1}, which is more difficult to overcome than that of CH_3CH_2O. Finally, CH_3CH_2O hydrogenation to ethanol (R32) *via* TS32 has an activation barrier of 114.1 kJ mol^{-1}, which is lower than that on the Cu(211) surface (127.1 kJ mol^{-1})[13] and MnCu(211) surface (261.8 kJ mol^{-1}),[78] suggesting that the addition of Fe can enhance the catalytic activity toward CH_3CH_2OH formation.

3.4 Microkinetic modeling

Microkinetic modeling[86–89] has been widely employed to investigate the activity and selectivity of catalysts. In this section, microkinetic modeling on the FeCu(211) surface was performed to estimate the rates of the products CH_3OH (r_{CH_3OH}), CH_4 (r_{CH_4}), and C_2H_5OH (r_{CH_3OH}), as well as their relative selectivity under typical experimental conditions (P_{CO} = 4 atm, P_{H_2} = 8 atm, and T = 500–600 K). The detailed description of the microkinetic model is given in the ESI.†

In the microkinetic modeling, the pseudo-steady-state approximation[79] was applied to the other minority species on the catalyst surface, and the production rates and the consumption rates of all the species were assumed to be in equilibrium. Table S2 (ESI†) lists all the elementary steps involved in the optimal formation pathways of CH_3OH, CH_4, and C_2H_5OH, as well as the corresponding rate constants at 500, 525, 550, 575, and 600 K. Fig. 11 presents the relative selectivity of the products CH_4, CH_3OH, and C_2H_5OH in syngas conversion on the FeCu(211) surface at different temperatures.

On the FeCu(211) surface, the productivity of C_2H_5OH ($r_{CH_3CH_2OH}$ = 4.68 × 10^{-2} s^{-1} $site^{-1}$) is higher than that of CH_3OH (r_{CH_3OH} = 3.27 × 10^{-2} s^{-1} $site^{-1}$) and CH_4 (r_{CH_4} = 8.87 × 10^{-4} s^{-1} $site^{-1}$) at 500 K. The relative selectivity of C_2H_5OH can reach 53–58% at 500–600 K, which is higher than CH_3OH, while the value for CH_4 is negligible. This result is consistent with previous experimental results,[20,90] suggesting that the high dispersion of active species and the Cu–Fe synergistic

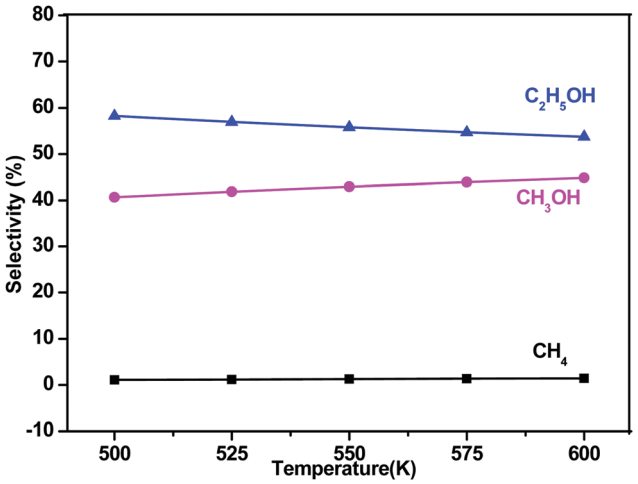

Fig. 11 Relative selectivity of the products CH_4, CH_3OH, and C_2H_5OH in syngas conversion on the FeCu(211) surface at different temperatures using microkinetic modeling.

effect together improve the alcohol selectivity, especially C_2–C_5 alcohols, and decrease the selectivity of methanol and methane. As a result, the CuFe bimetallic catalyst shows a high productivity and selectivity toward ethanol formation.

3.5 General discussion

3.5.1 The active sites of the FeCu(211) surface. The above results show that all the species and all the elementary reactions in ethanol formation from syngas prefer to occur at the Fe site or at the sites consisting of Fe and Cu atoms over the FeCu(211) surface. Moreover, for C_2 oxygenates formation *via* CO insertion into CH_x (x = 2, 3), CO prefers to adsorb at the Fe site, while CH_x (x = 2, 3) is adsorbed at the Fe site or the sites consisting of Fe and Cu atoms, indicating that the surface Cu sites or Fe site over the FeCu(211) surface are the active sites, and the synergetic effect between Fe and Cu plays an important role in determining the selectivity in ethanol formation from syngas, which agrees with the previous experimental results.[33,39]

3.5.2 The role of Fe. In order to clarify the role of Fe in ethanol synthesis on the FeCu bimetallic catalyst, the electronic properties of the Fe atom and its surrounding Cu atoms was analyzed. The differential charge density plot in Fig. 12 shows the electron transfers from the surface Fe to Cu, while the Bader charge analysis shows that the number of electrons transferred is 0.15 e, suggesting that the addition of Fe has an effect on the electronic properties rather than on the geometry of the ensembles. In addition, previous studies[10,78] proved that the addition of Rh or Mn into a Cu catalyst facilitated CH_3 formation in syngas conversion. Moreover, the addition of Co into a Cu catalyst[18] promoted the formation of CH_x (x = 2, 3), which provided more CH_x resources for the C–C chain due to a bimetallic synergetic effect. Thus, in this study, the synergetic effect between Fe and Cu improves the selectivity toward the formation of CH_x (x = 2, 3), C_2 oxygenates, and ethanol in syngas conversion over the Fe-decorated Cu bimetallic catalyst.

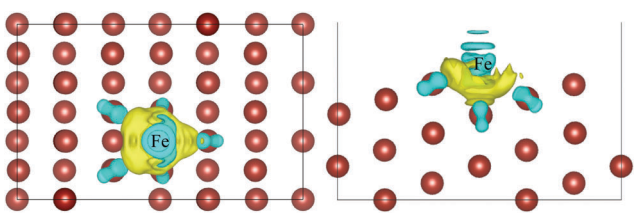

Fig. 12 Differential charge density of an Fe atom and its surrounding Cu atoms over the FeCu(211) surface. The blue and yellow shaded regions represent the charge loss and charge gain, respectively.

4. Conclusions

In summary, periodic DFT calculations together with microkinetic modeling were used to investigate the reaction mechanism of C_2 oxygenate and ethanol formation from syngas on the FeCu(211) surface. The results show that the initial adsorption and activation of CO occur at the Fe site, and that CO prefers to be hydrogenated to CHO. Starting from CHO species, CH_2 is formed by the pathway CHO + H → CH_2O + H → CH_2OH → CH_2 + OH, which is more favorable than CH_3OH formation, both thermodynamically and dynamically. In addition, CH_2 and CH_3 species can convert each other, and are major CH_x species on the FeCu(211) surface. C_2 oxygenates CH_2CO, and CH_3CO are dominantly formed by CO insertion into CH_2 and CH_2CO hydrogenation instead of C_2 hydrocarbons or CH_4; then, CH_2CO and CH_3CO are successively hydrogenated to ethanol. Moreover, microkinetic modeling shows that the FeCu(211) surface exhibits a high selectivity toward ethanol formation rather than methanol and methane. Fe in the FeCu bimetal catalyst mainly promotes CH_x formation by accelerating C–O bond cleavage, and also suppresses methanol formation and facilitates the formation of C_2 oxygenates.

Conflicts of interest

There are no conflicts to declare.

Acknowledgements

This work is financially supported by the Key projects of National Natural Science Foundation of China (20736007), National Natural Science Foundation of China (No. 21476155, 21576178, 21776193), the Program for the Top Young Academic Leaders of Higher Learning Institutions of Shanxi, and the Top Young Innovative Talents of Shanxi.

References

1 J. J. Spivey and A. Egbebi, *Chem. Soc. Rev.*, 2007, **36**, 1514–1528.
2 R. G. Herman, *Catal. Today*, 2000, **55**, 233–245.
3 K. G. Fang, D. B. Li, M. G. Lin, M. L. Xiang, W. Wei and Y. H. Sun, *Catal. Today*, 2009, **147**, 133–138.
4 P. Forzatti, E. Tronconi and I. Pasquon, *Catal. Rev.: Sci. Eng.*, 1991, **33**, 109–168.

5 V. R. Surisetty, A. K. Dalai and J. Kozinski, *Appl. Catal., A*, 2011, **404**, 1–11.
6 J. J. Scheibel, *J. Surfactants Deterg.*, 2004, **7**, 319–328.
7 V. Subramani and S. K. Gangwal, *Energy Fuels*, 2008, **22**, 814–839.
8 H. Kusama, K. Okabe, K. Sayama and H. Arakawa, *Appl. Organomet. Chem.*, 2000, **14**, 836–840.
9 S. F. Zaman and K. J. Smith, *Catal. Today*, 2011, **171**, 266–274.
10 R. G. Zhang, M. Peng and B. J. Wang, *Catal. Sci. Technol.*, 2017, **7**, 1073–1085.
11 Y. Yang, Y. D. Wang, S. Liu, Q. Y. Song, Z. K. Xie and Z. Gao, *Catal. Lett.*, 2009, **127**, 448–455.
12 S. Zaman and K. J. Smith, *Catal. Rev.*, 2012, **54**, 41–132.
13 R. G. Zhang, G. R. Wang and B. J. Wang, *J. Catal.*, 2013, **305**, 238–255.
14 Z. J. Zuo, L. Wang, Y. J. Liu and W. Huang, *Catal. Commun.*, 2013, **34**, 69–72.
15 Y. Y. Liu, K. Murata, M. Inaba, I. Takahara and K. Okabe, *Fuel*, 2013, **104**, 62–69.
16 R. G. Zhang, M. Peng, T. Duan and B. J. Wang, *Appl. Surf. Sci.*, 2017, **407**, 282–296.
17 Y. W. Lu, R. G. Zhang, B. B. Cao, B. H. Ge, F. F. Tao, J. J. Shan, L. Nguyen, Z. H. Bao, T. P. Wu, J. W. Pote, B. J. Wang and F. Yu, *ACS Catal.*, 2017, **7**, 5500–5512.
18 R. G. Zhang, F. Liu and B. J. Wang, *Catal. Sci. Technol.*, 2016, **6**, 8036–8054.
19 H. Y. Zheng, R. G. Zhang, Z. Li and B. J. Wang, *J. Mol. Catal. A: Chem.*, 2015, **404**, 115–130.
20 G. Lin, K. G. Fang, D. D. Li and Y. H. Sun, *Catal. Commun.*, 2008, **9**, 1869–1873.
21 Y. W. Lu, F. Yu, J. Hu and J. Liu, *Appl. Catal., A*, 2012, **429**, 48–58.
22 X. Dong, X. L. Liang, H. Y. Li, G. D. Lin, P. Zhang and H. B. Zhang, *Catal. Today*, 2009, **147**, 158–165.
23 N. T. Thao and M. H. Zahedi-Niaki, *J. Catal.*, 2007, **245**, 348–357.
24 J. Iranmahboob, H. Toghiani, D. O. Hill and F. Nadim, *J. Catal.*, 2002, **79**, 71–75.
25 R. G. Zhang, X. C. Sun and B. J. Wang, *J. Phys. Chem. C*, 2013, **117**, 6594–6606.
26 K. Xiao, Z. H. Bao, X. Z. Qi, X. X. Wang, L. S. Zhong, K. G. Fang, M. G. Lin and Y. H. Sun, *Chin. J. Catal.*, 2013, **34**, 116–129.
27 H. J. Guo, L. Xiong, C. R. Luo, F. Ding, X. D. Chen and Y. Chen, *Acta Phys.-Chim. Sin.*, 2011, **27**, 2632–2638.
28 M. Y. Ding, J. L. Tu, M. H. Qiu, T. J. Wang, L. L. Ma and Y. P. Li, *Appl. Energy*, 2015, **138**, 584–589.
29 H. Zhang, W. Chu, H. Y. Xu and J. Zhou, *Fuel*, 2010, **89**, 3127–3131.
30 D. S. Mao, Q. S. Guo, J. Yu, L. P. Han and G. Z. Lu, *Acta Phys.-Chim. Sin.*, 2011, **27**, 2639–2645.
31 M. G. Lin, K. G. Fang, D. B. Li and Y. H. Sun, *Acta Phys.-Chim. Sin.*, 2008, **24**, 833–838.
32 J. G. Liu, M. Y. Ding, T. J. Wang and L. L. Ma, *Acta Phys.-Chim. Sin.*, 2012, **28**, 1964–1970.
33 Y. H. Zhao, S. G. Li and Y. H. Sun, *J. Phys. Chem. C*, 2013, **117**, 24920–24931.
34 X. X. Tian, T. Wang, Y. Yang, Y. W. Li, J. G. Wang and H. J. Jiao, *J. Phys. Chem. C*, 2014, **118**, 20472–20480.
35 X. H. Zhao, Y. W. Li, J. Wang and C. F. Huo, *J. Fuel Chem. Technol.*, 2011, **39**, 956–960.
36 M. Elahifard, E. Fazeli, A. Joshani and M. Gholami, *Surf. Interface Anal.*, 2013, **45**, 1081–1087.
37 X. D. Xu, E. B. M. Doesburg and J. J. F. Scholten, *Catal. Today*, 1987, **2**, 125–170.
38 R. Xu, Y. Cheng, W. Wei, W. H. Li, Y. H. Sun and T. D. Hu, *J. Mol. Catal. A: Chem.*, 2004, **221**, 51–58.
39 M. Y. Ding, M. H. Qiu, T. J. Wang, L. L. Ma, C. Z. Wu and J. G. Liu, *Appl. Energy*, 2012, **97**, 543–547.
40 A. F. H. Wielers, C. E. C. A. Hop, J. van Beijnum, A. M. van der Kraan and J. W. Geus, *J. Catal.*, 1990, **121**, 364–374.
41 Z. H. Chonco, A. Ferreira, L. Lodya, M. Claeys and E. van Steen, *J. Catal.*, 2013, **307**, 283–294.
42 Z. H. Chonco, L. Lodya, M. Claeys and E. van Steen, *J. Catal.*, 2013, **308**, 363–373.
43 H. J. Wan, B. S. Wu, C. H. Zhang, H. W. Xiang and Y. W. Li, *J. Mol. Catal. A: Chem.*, 2008, **283**, 33–42.
44 X. M. Yang, Y. Wei, Y. L. Su and L. P. Zhou, *Fuel Process. Technol.*, 2010, **91**, 1168–1173.
45 O. L. J. Gijzeman, T. J. Vink, O. P. van Pruissen and J. W. Geus, *J. Vac. Sci. Technol., A*, 1987, **5**, 718–721.
46 S. R. Goodman, S. S. Brenner and J. R. Low, *Metall. Trans.*, 1973, **4**, 2371–2378.
47 M. A. Turchanin, P. G. Agraval and I. V. Nikolaenko, *J. Phase Equilib.*, 2003, **24**, 307–319.
48 X. X. Tian, T. Wang, Y. Yang, Y. W. Li, J. G. Wang and H. J. Jiao, *J. Phys. Chem. C*, 2014, **118**, 21963–21974.
49 X. X. Tian, T. Wang, Y. Yang, Y. W. Li, J. G. Wang and H. J. Jiao, *Phys. Chem. Chem. Phys.*, 2014, **16**, 26997–27011.
50 X. X. Tian, T. Wang, Y. Yang, Y. W. Li, J. G. Wang and H. J. Jiao, *J. Phys. Chem. C*, 2015, **119**, 7371–7385.
51 S. Eric van and C. Michael, *Catal., Struct. React.*, 2015, **1**, 11–18.
52 S. X. Yin, X. Y. Ma and D. E. Ellis, *Surf. Sci.*, 2007, **601**, 2426–2437.
53 J. A. Rodriguez, J. C. Hanson, A. I. Frenkel, J. Y. Kim and M. Pérez, *J. Am. Chem. Soc.*, 2002, **124**, 346–354.
54 Y. W. Lu, B. B. Cao, F. Yu, J. Liu, Z. H. Bao and J. S. Gao, *ChemCatChem*, 2014, **6**, 473–478.
55 J. Zhang, X. M. Cao, P. Hu, Z. Y. Zhong, A. Borgna and P. Wu, *J. Phys. Chem. C*, 2011, **115**, 22429–22437.
56 T. Zamvelli, J. Wintterlin, J. Throst and G. Ertl, *Science*, 1996, **273**, 1688–1690.
57 R. C. Catapan, A. A. M. Oliveira, Y. Chen and D. G. Vlachos, *J. Phys. Chem. C*, 2012, **116**, 20281–20291.
58 M. Mavrikakis, M. Bäumer, H. J. Freund and J. K. Nørskov, *Catal. Lett.*, 2002, **81**, 153–156.
59 Y. Xu and M. Mavrikakis, *J. Phys. Chem. B*, 2003, **107**, 9298–9307.
60 N. Kapur, J. Hyun, B. Shan, J. B. Nicholas and K. Cho, *J. Phys. Chem. C*, 2010, **114**, 10171–10182.
61 M. Behrens, F. Studt, I. Kasatkin, S. Kühl, M. Hävecker, F. Abild-Pedersen, S. Zander, F. Girgsdies, P. Kurr, B. L. Kniep, M. Tovar, R. W. Fischer, J. K. Nørskov and R. Schlögl, *Science*, 2012, **336**, 893–897.

62 G. Kresse and J. Hafner, *Phys. Rev. B: Condens. Matter Mater. Phys.*, 1993, **48**, 13115–13118.
63 G. Kresse and J. Furthmüller, *Phys. Rev. B: Condens. Matter Mater. Phys.*, 1996, **54**, 11169–11186.
64 P. E. Blöchl, *Phys. Rev. B: Condens. Matter Mater. Phys.*, 1994, **50**, 17953–17979.
65 G. Kresse and D. Joubert, *Phys. Rev. B: Condens. Matter Mater. Phys.*, 1999, **59**, 1758–1775.
66 J. P. Perdew, K. Burke and M. Ernzerhof, *Phys. Rev. Lett.*, 1996, **77**, 3865–3868.
67 J. P. Perdew and Y. Wang, *Phys. Rev. B: Condens. Matter Mater. Phys.*, 1992, **45**, 13244–13249.
68 S. G. Louie, S. Froyen and M. L. Cohen, *Phys. Rev. B: Condens. Matter Mater. Phys.*, 1982, **26**, 1738–1742.
69 Q. Ge, M. Neurock, H. A. Wright and N. Srinivasan, *J. Phys. Chem. B*, 2002, **106**, 2826–2829.
70 L. Joos, I. A. W. Filot, S. Cottenier, E. J. M. Hensen, M. Waroquier, V. V. Speybroeck and R. A. van Santen, *J. Phys. Chem. C*, 2014, **118**, 5317–5327.
71 D. Sheppard, P. Xiao, W. Chemelewski, D. D. Johnson and G. Henkelman, *J. Chem. Phys.*, 2012, **136**, 074103.
72 D. Sheppard, R. Terrell and G. Henkelman, *J. Chem. Phys.*, 2008, **128**, 134106.
73 G. Henkelman and H. Jónsson, *J. Chem. Phys.*, 1999, **111**, 7010–7022.
74 R. A. Olsen, G. J. Kroes, G. Henkelman, A. Arnaldsson and H. Jónsson, *J. Chem. Phys.*, 2004, **121**, 9776–9792.
75 W. P. Ma, E. L. Kugler and D. B. Dadyburjor, *Energy Fuels*, 2011, **25**, 1931–1938.
76 J. P. Clay, J. P. Greeley, F. H. Ribeiro, W. N. Delgass and W. F. Schneider, *J. Catal.*, 2014, **320**, 106–117.
77 Y. H. Zhao, M. M. Yang, D. P. Sun, H. Y. Su, K. J. Sun, X. F. Ma, X. H. Bao and W. X. Li, *J. Phys. Chem. C*, 2011, **115**, 18247–18256.
78 M. Ojeda, R. Nabar, A. U. Nilekar, A. Ishikawa, M. Mavrikakis and E. Iglesia, *J. Catal.*, 2010, **272**, 287–297.
79 S. Shetty, A. P. J. Jansen and R. A. van Santen, *J. Am. Chem. Soc.*, 2009, **131**, 12874–12875.
80 R. G. Zhang, G. R. Wang, B. J. Wang and L. X. Ling, *J. Phys. Chem. C*, 2014, **118**, 5243–5254.
81 J. C. Wang, Z. X. Liu, R. G. Zhang, G. R. Wang and B. J. Wang, *J. Phys. Chem. C*, 2014, **118**, 22691–22701.
82 Y. M. Choi and P. Liu, *J. Am. Chem. Soc.*, 2009, **131**, 13054–13061.
83 N. Kapur, J. Hyun, B. Shan, J. B. Nicholas and K. Cho, *J. Phys. Chem. C*, 2010, **114**, 10171–10182.
84 L. C. Grabow and M. Mavrikakis, *ACS Catal.*, 2011, **1**, 365–384.
85 F. Studta, F. Abild-Pedersena, Q. X. Wu, A. D. Jensen, B. Temel, J. D. Grunwaldte and J. K. Nørskov, *J. Catal.*, 2012, **293**, 51–60.
86 P. Liu, A. Logadottir and J. K. Nørskov, *Electrochim. Acta*, 2003, **48**, 3731–3742.
87 P. Liu and J. A. Rodriguez, *J. Chem. Phys.*, 2007, **126**, 164705.
88 P. Liu and J. A. Rodriguez, *J. Phys. Chem. B*, 2006, **110**, 19418–19425.
89 Y. M. Choi and P. Liu, *J. Am. Chem. Soc.*, 2009, **36**, 13054–13061.
90 W. Gao, Y. F. Zhao, J. M. Liu, Q. W. Huang, S. He, C. M. Li, J. W. Zhao and M. Wei, *Catal. Sci. Technol.*, 2013, **3**, 1324–1332.